Electronic Supplementary Material (ESI) for Sustainable Energy & Fuels.

Support information

Self-woven nanofibrillar PEDOT mats for impact-resistant supercapacitors

Hongmin Wang, [a] Luciano M. Santino, [a] Micah. Rubin, [a] Yifan Diao, [b] Yang Lu, [b] and Julio M. D'Arcy *[ab]

[a] Department of Chemistry, Washington University in St. Louis, St. Louis, Missouri 63130, United States

[b] Institute of Materials Science & Engineering, Washington University in St. Louis, St. Louis, Missouri 63130, United States

Table S1. Summary of conducting nanofibrillar mats

Material	Synthesis methods	Conductivity (S/cm)	Sheet resistance (Ω/square)	Ref
Nanofibrillar PEDOT mats	Hydrolysis-assisted VPP	334	1.3	This work
PEDOT nanotube	PMMA templated VDP	2 – 60	–	1
PEDOT:PSS-PVA	Electrospinning	1.7×10^{-5}	–	2
PEDOT nanofibers	Electrospinning & VPP	60	–	3
PEDOT:PSS nanofibers	Electrospinning	–	18000	4
PEDOT nanofibers	Ternary phase synthesis	137	–	5
PEDOT nanowires	PAA templated synthesis	0.56	–	6
PEDOT/Bacterial cellulose	Solution synthesis	1.3×10^{-3}	–	7
PEDOT/Carbon cloth	Electrospinning & solution synthesis	90	–	8
PEDOT nanofibers	Electrospinning & VPP	72	–	9
PANi/PAA	Electrospinning	0.14	–	10
PANi	Electrospinning	0.11	–	11
PANi-CNT	Electrospinning	0.15	–	11
PANi/Nafion	Electrospinning	0.01	–	12
PANi/PA6/N-CNT_{650}	Electrospinning	0.12	–	13
PPy/PEO	Electrospinning	0.01	–	14

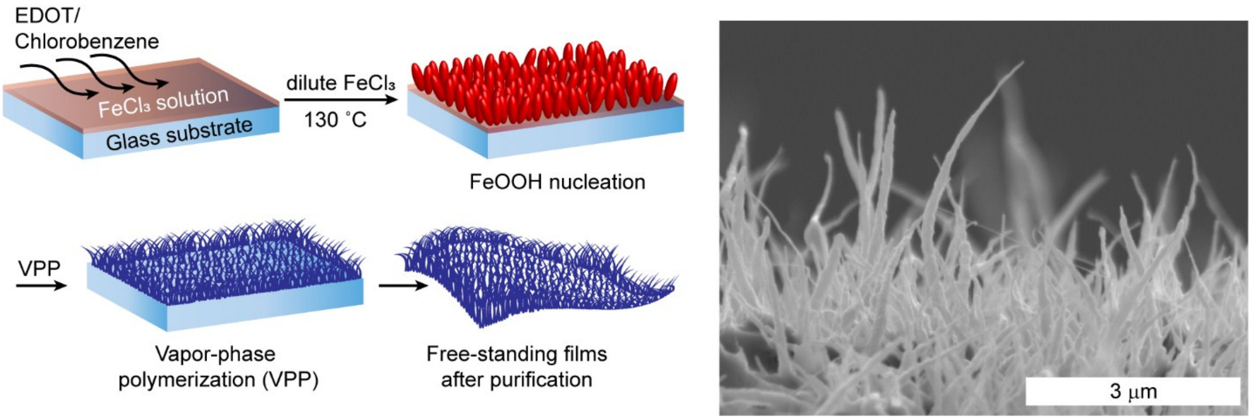

Figure S1. Schematic illustration of mechanism for vertically directed nanofibre formation and scanning electron micrograph profile of a vertically directed nanofibrillar PEDOT film.

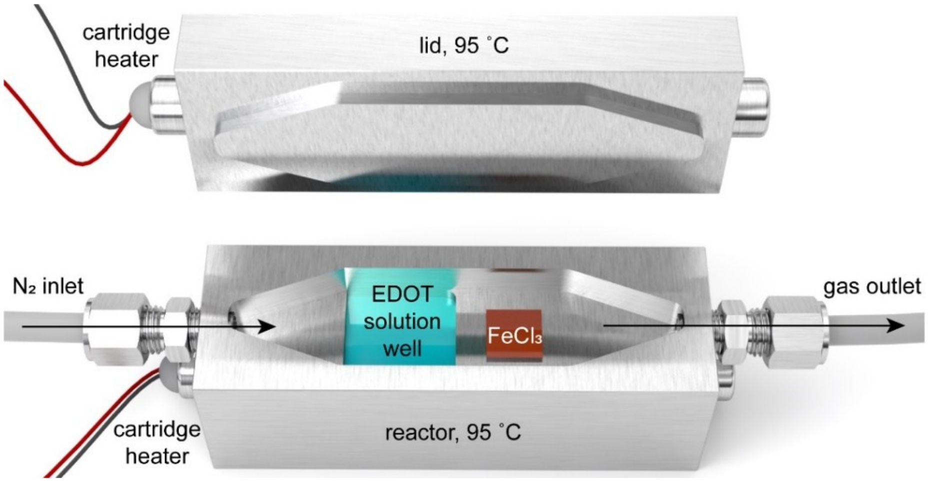

Figure S2. Chemical vapor deposition reactor for vapor-phase polymerization.

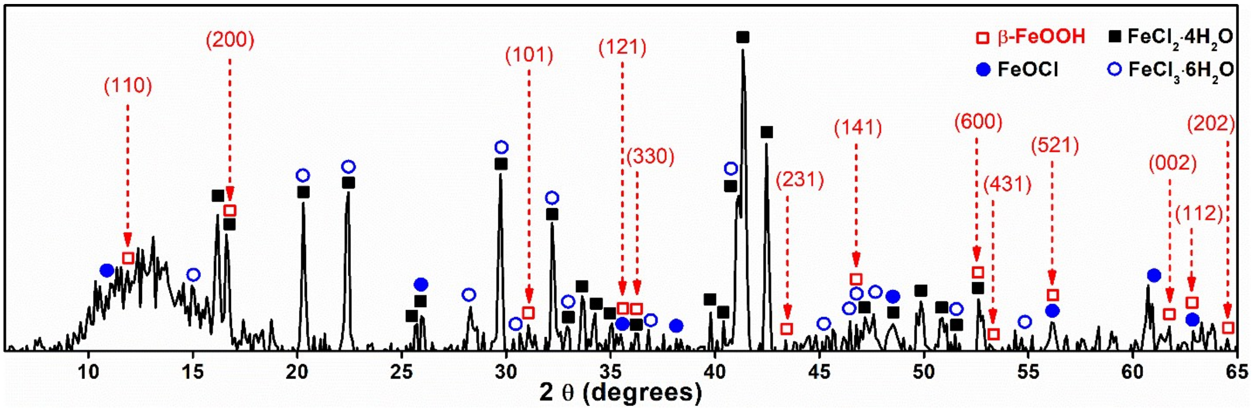

Figure S3. Powder X-ray diffraction spectrum of synthesis quenched 5 min after temperature reaches 95 °C; this shows the presence of multiple inorganic phases including β-FeOOH, FeOCl, $FeCl_2 \cdot 4H_2O$ and $FeCl_3 \cdot 6H_2O$. β-FeOOH crystal planes are labeled.

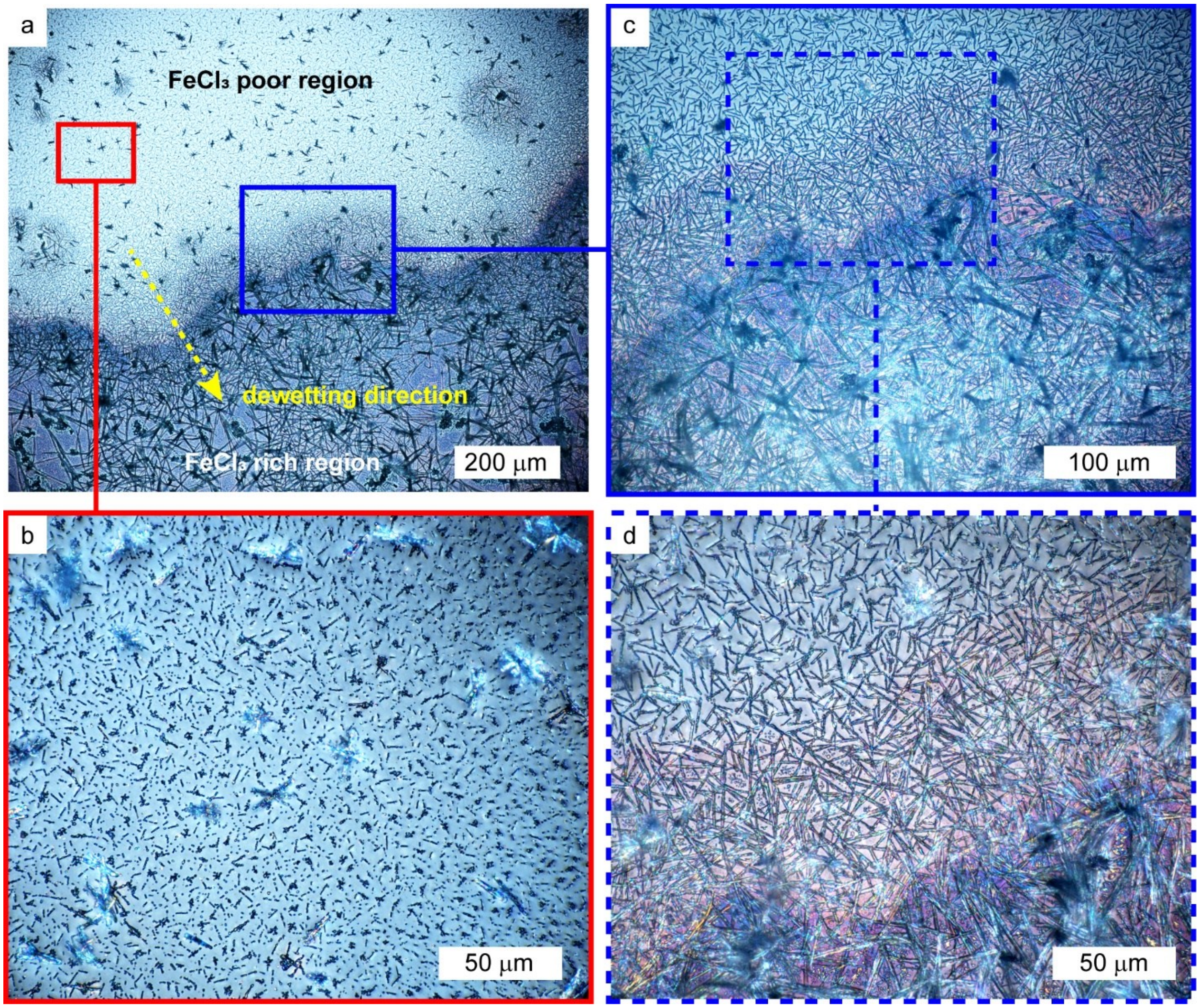

Figure S4. Optical micrographs of a PEDOT-coated substrate collected after completion of synthesis along the dewetting direction of the oxidant liquid film. Lighter color in (a) indicates a lower concentration of $FeCl_3$ due to dewetting that causes directional fluid flow and solute redistribution. Larger crystallites are observed in the bulk of a pinned liquid film where $FeCl_3$ concentration is higher than in the dewetted region. (b) Close-up of dewetted region shows anisotropic 1D nuclei quenched during the initial stages of reaction. (c-d) Close-ups of the interface between dewetted and pinned regions, show a gradient in size and packing density of asterisks that increases with $FeCl_3$ concentration.

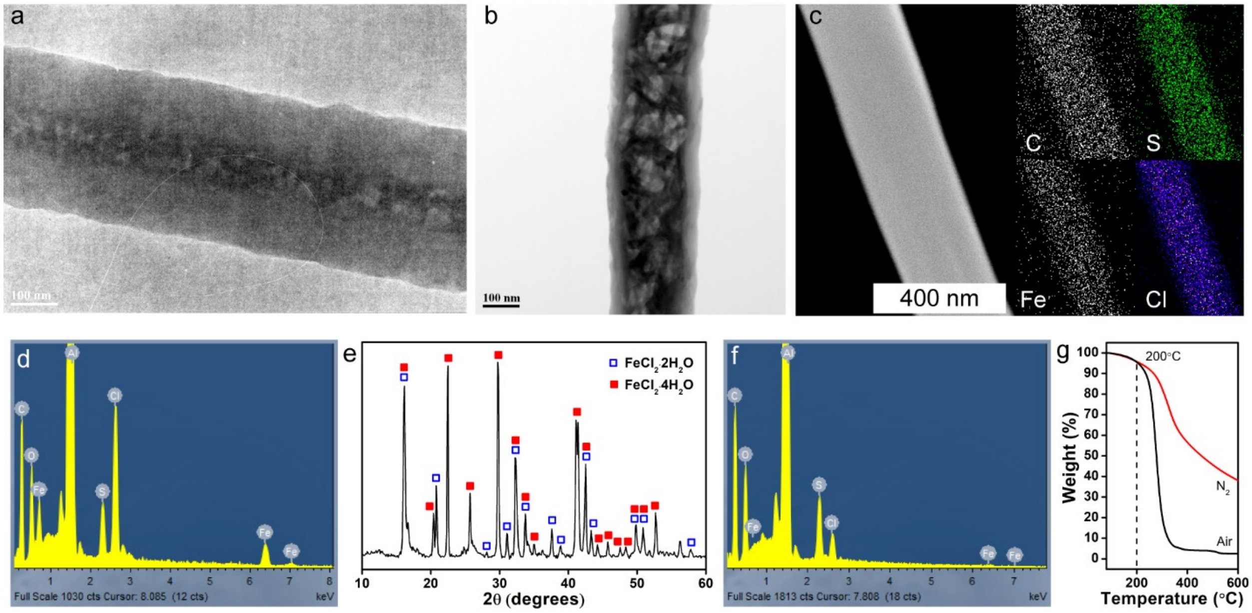

Figure S5. Transmission electron micrographs of PEDOT nanofibres show an (a) inorganic-organic core-shell structure that (b) reacts over time until it is completely consumed during oxidative radical vapor phase polymerization. (c-d) Energy-dispersive X-ray spectroscopy maps of as-synthesized nanofibres show elemental signals from C, S, Fe and Cl. (e) Powder X-ray diffraction spectrum shows Fe signals from $FeCl_2$, the reduced oxidant byproduct. (f) After purification in acid, this Fe signal is undetectable via energy-dispersive X-ray spectroscopy. (g) Thermogravimetric analysis of purified nanofibrillar PEDOT mats in both air and N_2 indicate good thermal stability up to 200 °C with minimal weight loss before 200 °C.

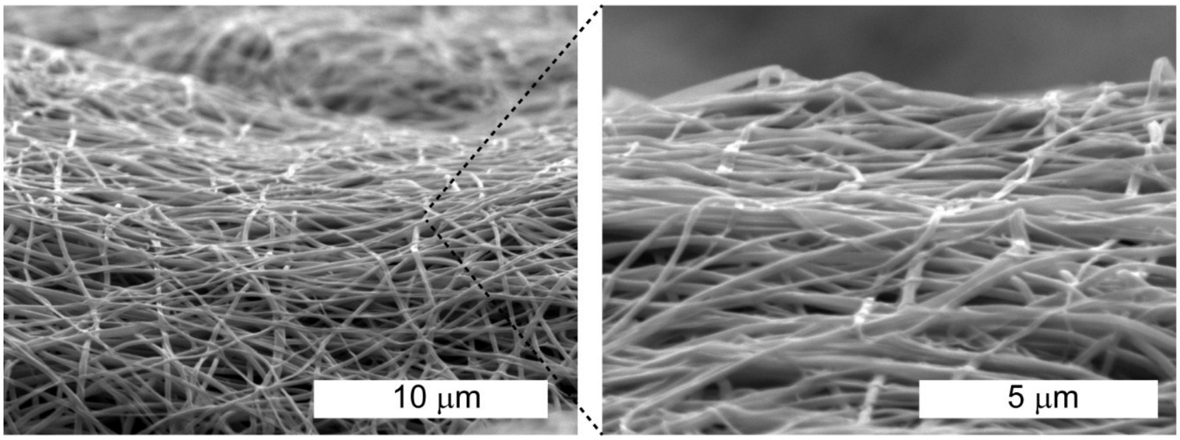

Figure S6. Close-up SEM sequence of a nanofibrillar PEDOT mat. This tilted micrograph shows a membrane architecture comprised of horizontally directed interweaving nanofibres; a nanofibrillar PEDOT mat is characterized by high interfibrillar porosity.

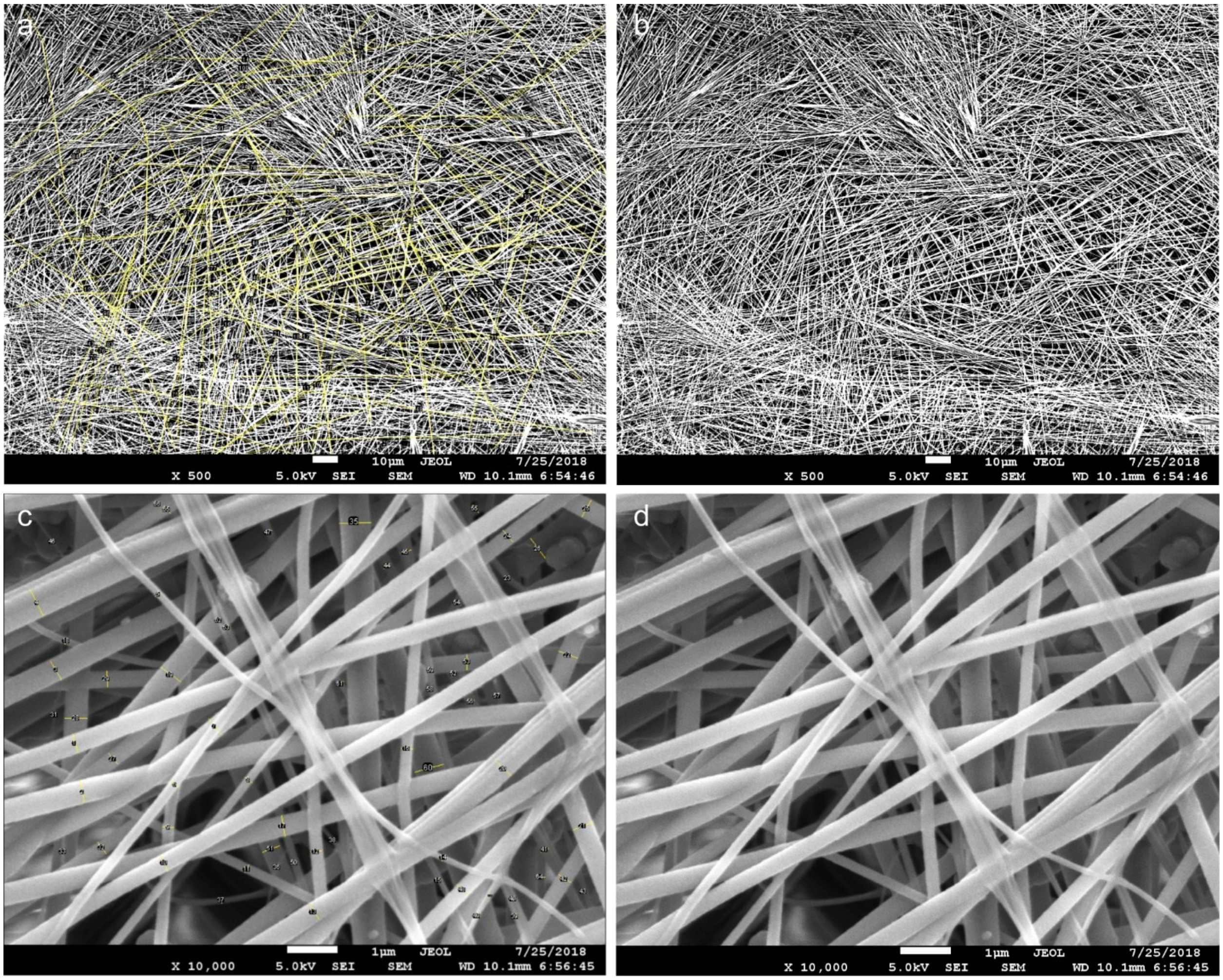

Figure S7. ImageJ is used to calculate and measure the nanofibre length and width from SEM images. (a) The lengths of 100 nanofibres are collected and averaged (marked with yellow lines). (b) Original SEM used for nanofibre length calculation. (c) The width of 66 nanofibres are collected (marked with yellow lines). (d) Original SEM used for nanofibre width calculation.

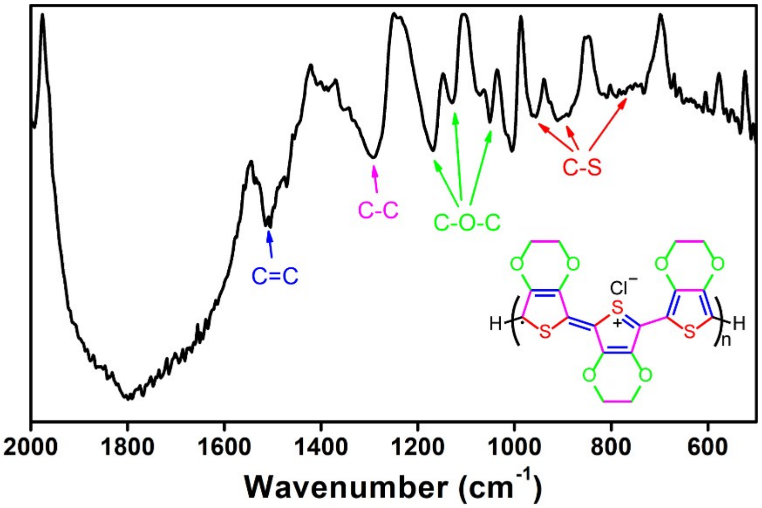

Figure S8. The molecular structure and doping of PEDOT is confirmed by Fourier-transform infrared spectroscopy. Finger print pattern shows strong absorption bands from C=C, C-C, C-O-C and C-S stretching.

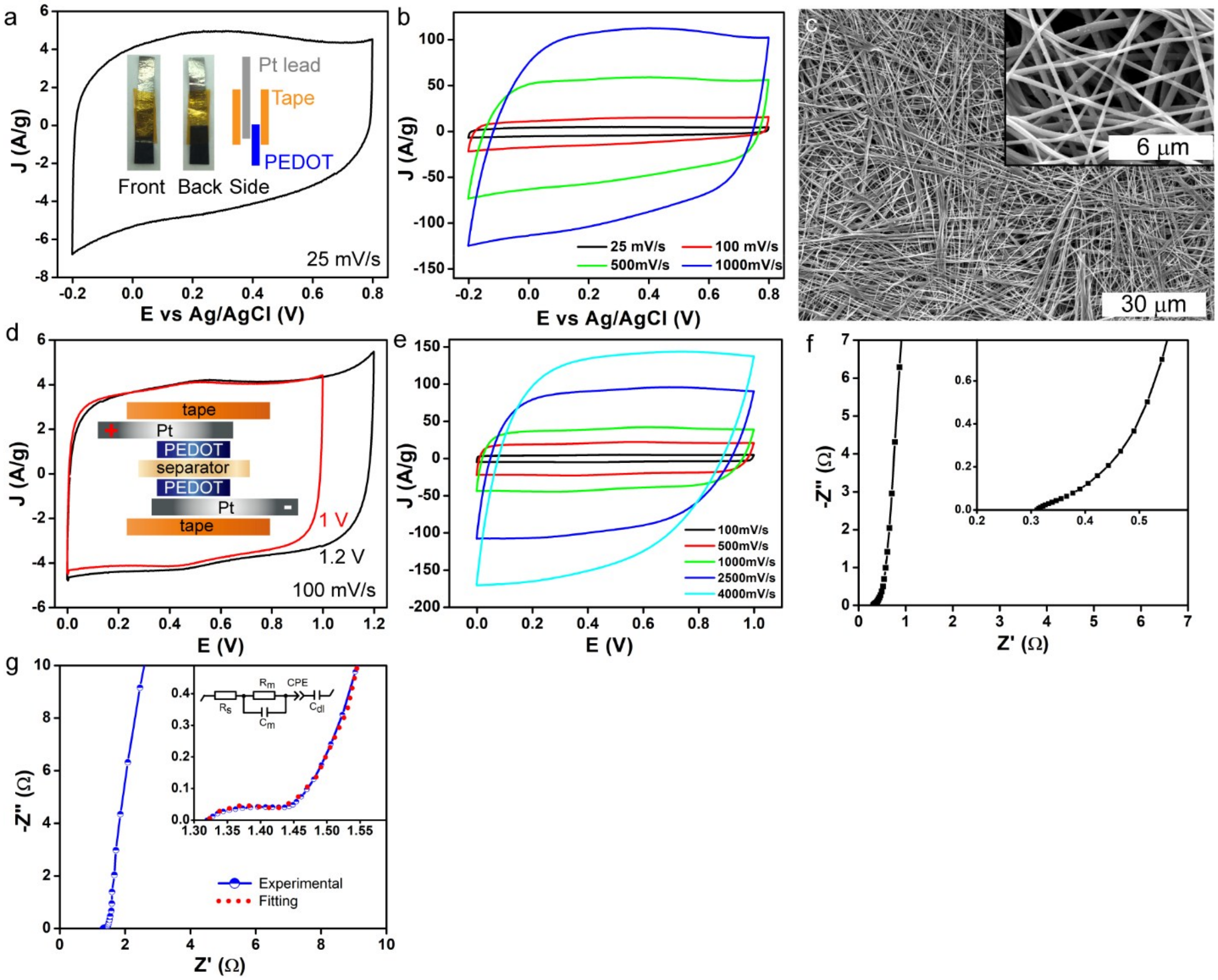

Figure S9. Electrochemical characterization of a nanofibrillar PEDOT mat. (a) Three-electrode cyclic voltammogram shows capacitive behavior at a scan rate of 25 mV/s (inset: working electrode exposes a 6.35× 6.35 mm area of PEDOT to the electrolyte). (b) Capacitive behavior continues up to a scan rate of 1000 mV/s due to fast charge transfer kinetics in our electrode. (c) The nanofibrillar morphology of PEDOT mat is unaffected and remains 1D even after 100 cycles at 1000 mV/s. (d) Two-electrode cyclic voltammogram at 100 mV/s shows rectangular shape at 1 and 1.2 V voltage window (inset: structure of the device, also shown in fig. 4a). (e) The rectangular shape is retained after scan rates increase to 4000mV/s. Electrochemical impedance spectroscopy Nyquist plots of (f) device and (g) three-electrode configuration shows capacitive behavior and internal resistance of 0.30 Ω and 1.32 Ω, respectively (inset: high frequency regions).

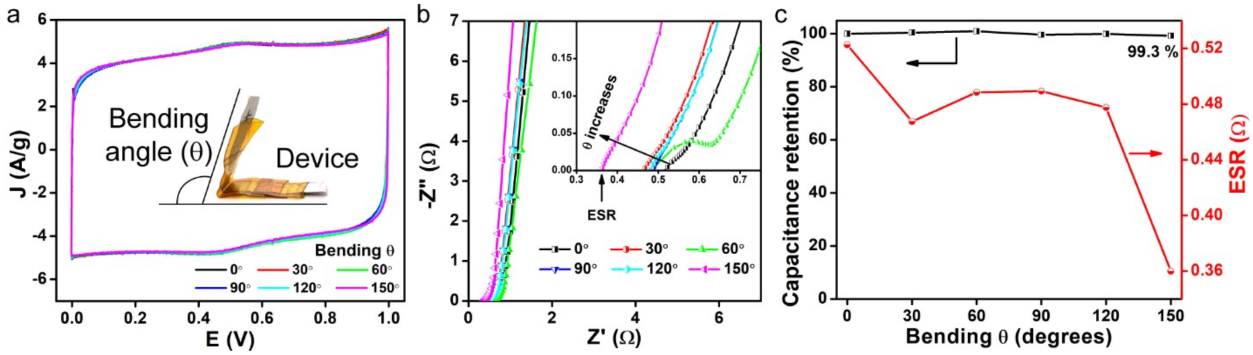

Figure S10. Bending tests for superactions. (a) A nanofibrillar PEDOT mat supercapacitor retains a rectangular shaped cyclic voltammogram even after bending at different angles; inset shows device and bending angle θ. (b-c) Nyquist plot and the equivalent series resistance demonstrate that upon bending capacitive behavior remains stable with little damage to electrode performance; resistance decreases slightly and 99.3% of original capacitance is retained after testing at a bending angle of θ = 150°.

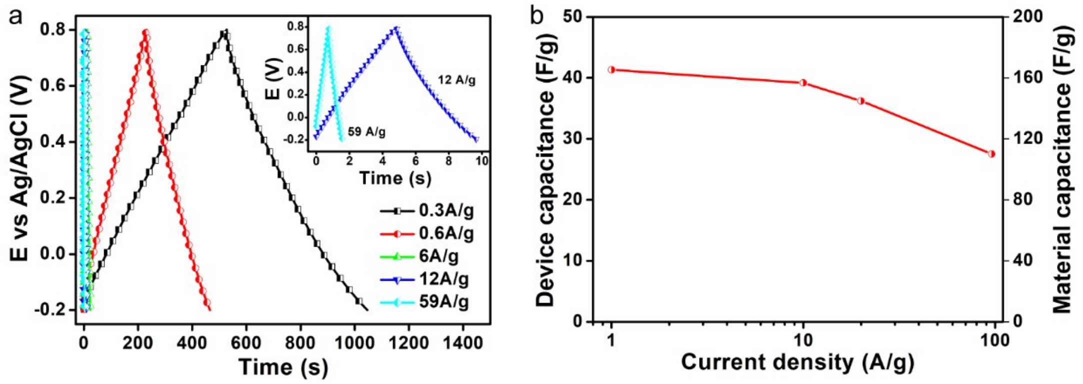

Figure S11. (a) Galvanostatic charge-discharge profiles recorded at different current densities show retention of triangular symmetry, this indicates facile charge transfer kinetics. (b) The device capacitance is calculated based on galvanostatic charge-discharge cycles and PEDOT mass at different current densities.

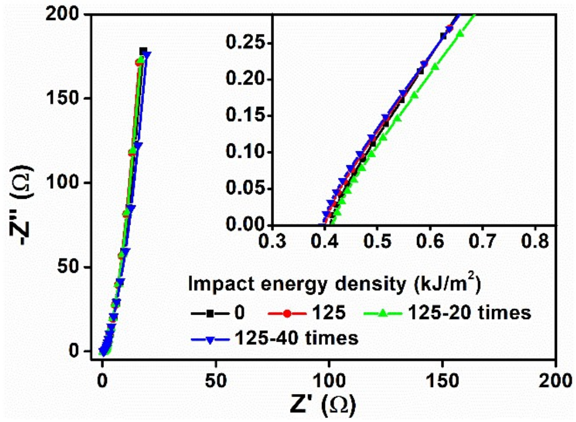

Figure S12. Nyquist plot shows that after repeated impacts, the capacitive behavior and equivalent series resistance remain stable.

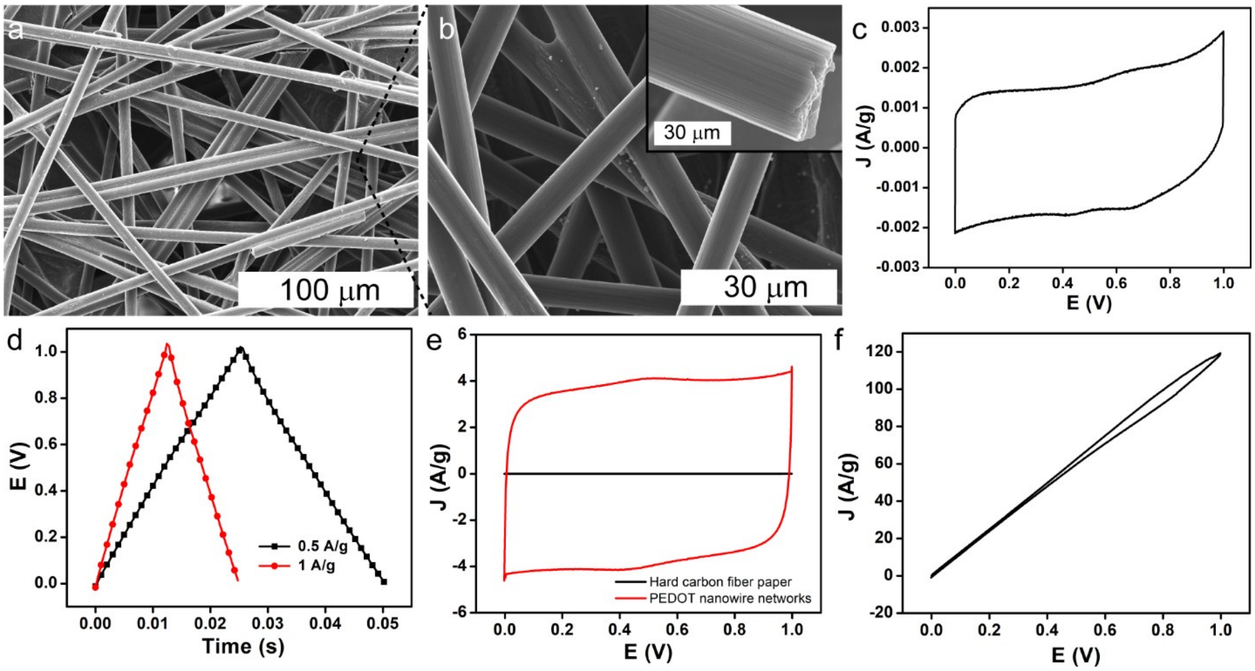

Figure S13. Morphology and energy storage properties of hard carbon fibre paper. (a-b) Close-up SEM images show horizontally directed architecture of carbon fibres of a hard carbon fibre paper substrate; these fibres are fragile and easily break (b inset). (c) Two-electrode cyclic voltammogram of device with configuration shown in Fig. 4a demonstrates minimal capacitive behavior as indicated by the low current. (d) Triangular galvanostatic charge-discharge curves at different current densities show a facile charge transfer. (e) Two-electrode cyclic voltammogram shows a negligible magnitude of capacitance for a hard carbon fibre paper substrate versus a nanofibrillar PEDOT mat. f) Supercapacitor fabricated using carbon fibre paper, serving both as active material and current collector, undergoes short circuit after experiencing a single mechanical impact of 4 kJ/m^2 impact energy density.

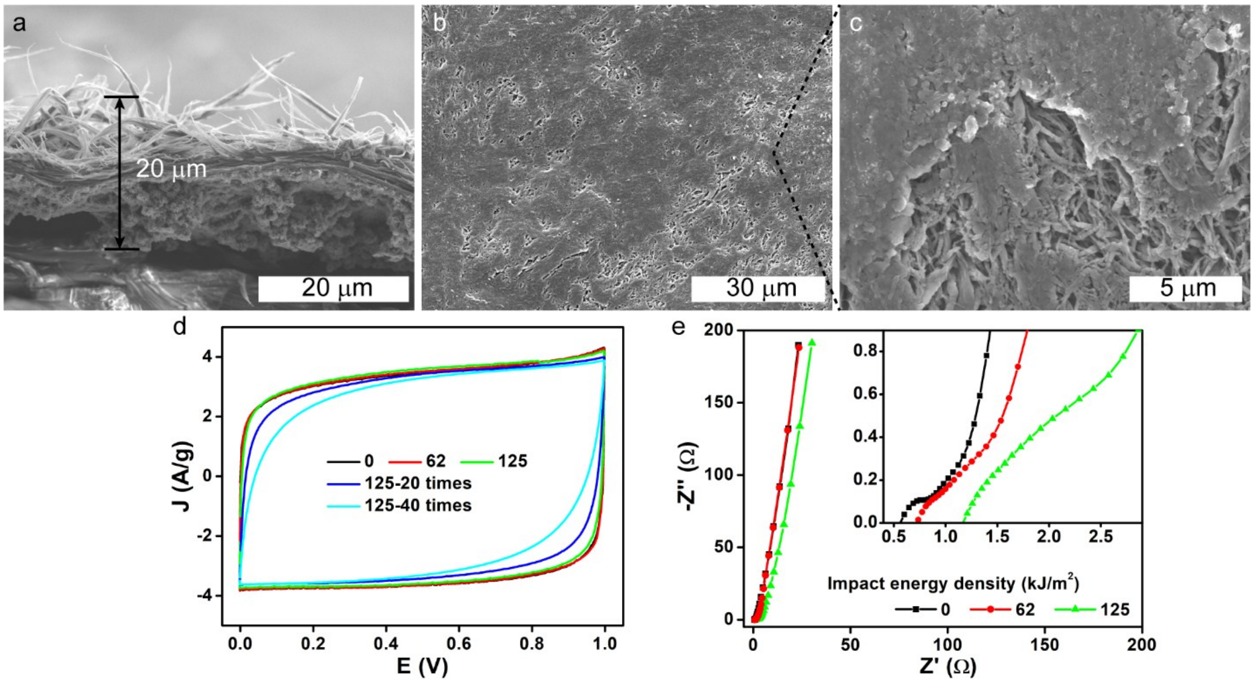

Figure S14. Vertically directed PEDOT nanofibre films in supercapacitors before and after impacts. (a) Cross-section of film before impact shows an average thickness of 20 μm. (b-c) Top-view of electrode after 40 impacts (125 kJ/m^2 impact energy density per impact) shows a deformed, dense and flattened morphology. (d) Two-electrode cyclic voltammogram indicate degradation of capacitance upon sequential impacts. (e) Nyquist plot demonstrates an increase in internal resistance and a decrease in capacitive behavior after repeated impacts.

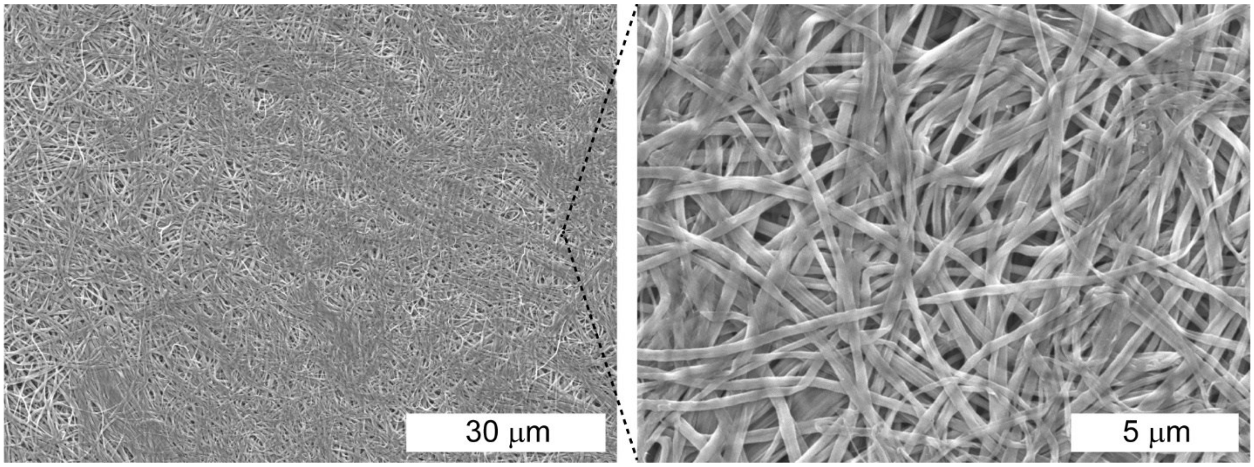

Figure S15. Close-up SEM images of horizontally directed nanofibrillar PEDOT mats in a supercapacitor after forty consecutive impacts with impact energy density of 125 kJ/m^2. Note that the interfibrillar porosity remains.

References

1. O. S. Kwon, S. J. Park, H.-W. Park, T. Kim, M. Kang, J. Jang and H. Yoon, *Chem. Mater.*, 2012, **24**, 4088-4092.
2. N. Liu, G. Fang, J. Wan, H. Zhou, H. Long and X. Zhao, *J. Mater. Chem.*, 2011, **21**, 18962.
3. A. Laforgue and L. Robitaille, *Macromolecules*, 2010, **43**, 4194-4200.
4. B. Bessaire, M. Mathieu, V. Salles, T. Yeghoyan, C. Celle, J. P. Simonato and A. Brioude, *ACS Appl. Mater. Interfaces.*, 2017, **9**, 950-957.
5. X. Bai, X. Hu, S. Zhou, J. Yan, C. Sun, P. Chen and L. Li, *J. Mater. Chem.*, 2011, **21**, 7123.
6. X. Sun and M. Hagner, *Macromolecules*, 2007, **40**, 8537-8539.
7. C. Chen, T. Zhang, Q. Zhang, Z. Feng, C. Zhu, Y. Yu, K. Li, M. Zhao, J. Yang, J. Liu and D. Sun, *ACS Appl. Mater. Interfaces.*, 2015, **7**, 28244-28253.
8. J. J. L. Guzman, M. O. Pehlivaner Kara, M. W. Frey and L. T. Angenent, *J. Power Sources*, 2017, **356**, 331-337.
9. H. Jiang, L. J. Halverson and L. Dong, *Journal of Micromechanics and Microengineering*, 2015, **25**, 125017.
10. M. A. Smirnov, E. V. Tarasova, V. K. Vorobiov, I. A. Kasatkin, V. Mikli, M. P. Sokolova, N. V. Bobrova, V. Vassiljeva, A. Krumme and A. V. Yakimanskiy, *J. Mater. Sci.*, 2018, **54**, 4859-4873.
11. S. K. Simotwo, C. DelRe and V. Kalra, *ACS Appl. Mater. Interfaces.*, 2016, **8**, 21261-21269.
12. S. K. Simotwo and V. Kalra, *Electrochim. Acta*, 2016, **198**, 156-164.
13. J. P. F. Santos, M. Arjmand, G. H. F. Melo, K. Chizari, R. E. S. Bretas and U. Sundararaj, *Materials & Design*, 2018, **141**, 333-341.
14. C. Shen, C.-P. Wang, M. Sanghadasa and L. Lin, *RSC Advances*, 2017, **7**, 11724-11731.